Research Square

Preprints are preliminary reports that have not undergone peer review.
They should not be considered conclusive, used to inform clinical practice,
or referenced by the media as validated information.

Mechanochemically covalently functionalized hexagonal boron nitride with proanthocyanidins for high-performance cellulose packaging toward fresh fruit preservation

Fatima Ait Aissa

LB01220927@sust.edu.cn

Shaanxi University of Science and Technology

Xue Jiang

Shaanxi University of Science and Technology

Xiuzhi Tian

Shaanxi University of Science and Technology

Research Article

Keywords: Hexagonal boron nitride sheets, Proanthocyanidins, Cellulose composite paper, Thermal conductivity, Antioxidant activity, Fruit preservation

Posted Date: November 3rd, 2026

DOI: https://doi.org/10.21203/rs.3.rs-10857072/v1

License: This work is licensed under a Creative Commons Attribution 4.0 International License.
Read Full License

Additional Declarations: No competing interests reported.

Mechanochemically covalently functionalized hexagonal boron nitride with proanthocyanidins for high-performance cellulose packaging toward fresh fruit preservation

Fatima Ait Aissa, Xue Jiang*, Xiuzhi Tian*

College of Bioresources Chemical and Materials Engineering, Shaanxi University of Science & Technology, Xi'an, Shaanxi, 710021, China.

Corresponding authors: **Fatima Ait Aissa (**LB01220927@sust.edu.cn), **Xue Jiang,** (jiangx@sust.edu.cn), **Xiuzhi Tian (**tianxz@sust.edu.cn).

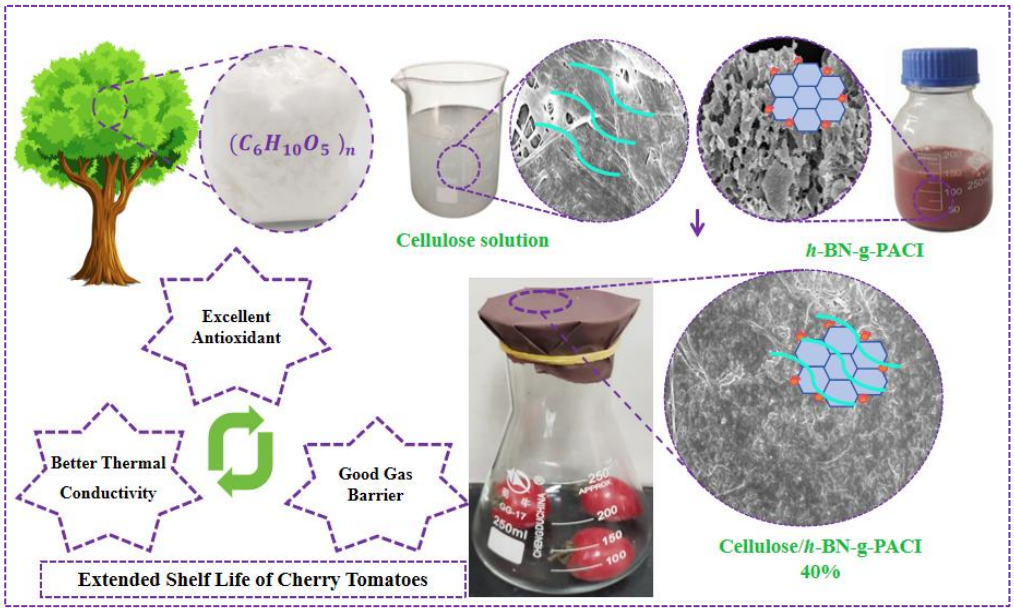
Abstract

Pristine cellulose paper is a biodegradable packaging material, yet it fails to regulate the internal microenvironment of fruit packages, lacking adequate antioxidant activity and sufficient gas/moisture barrier performance. Although hexagonal boron nitride (*h*-BN) and proanthocyanidins (PACI) can individually modify cellulose, PACI tends to self-aggregate in pulp and *h*-BN sheets stack severely, hindering uniform dispersion. We employ solvent-free mechanochemical ball-milling to graft PACI onto exfoliated few-layer *h*-BN, yielding *h*-BN-g-PACI hybrid fillers with a high grafting ratio of 66.7%. Comprehensive characterizations confirm the formation of stable B-O-C covalent linkages. The composite paper, fabricated via standard paper-making, with 40 wt% filler loading exhibits uniformly dispersed fillers, resulting in a tensile strength of 70 MPa (2.33 times that of pristine paper) and thermal conductivity of

1.954 W/m·K (6.76 times), alongside superior UV-shielding, surface hydrophobicity, and DPPH radical-scavenging activity. Moreover, the composite paper demonstrates improved resistance to moisture permeation. Ambient storage tests on cherry tomatoes reveal that the paper synergistically moderates temperature fluctuations, blocks moisture escape, and inhibits oxidative degradation, significantly reducing fruit weight loss, soluble solids accumulation, and mold growth. This scalable, eco-friendly fabrication approach offers a biodegradable multifunctional cellulose material as a promising alternative to petroleum-based plastic films for fresh fruit preservation.

Keywords: Hexagonal boron nitride sheets; Proanthocyanidins; Cellulose composite paper; Thermal conductivity; Antioxidant activity; Fruit preservation.

Graphical Abstract



Introduction

With the rapid expansion of fresh fruit e-commerce, biodegradable packaging materials that can extend the shelf life of seasonal fruits including grapes, strawberries, peaches and cherry tomatoes are urgently required. Fresh fruits are high-moisture respiratory horticultural products, which are susceptible to microbial contamination, enzymatic browning, moisture loss, shriveling and rot under ambient storage conditions **(Chan et al. 2025; Nian et al. 2024; Rajwar et al. 2016; Lufu et al. 2020; Gidado et al. 2024)**. Traditional petroleum-derived plastic packages can slightly delay fruit senescence, yet they bring severe long-term environmental pollution **(Ncube et al. 2020; Yin et al. 2024; Mahajan et al. 2014)**. In addition, their highly sealed structure tends to trap internal heat and water vapor, thereby accelerating mold proliferation and fruit deterioration.

Cellulose serves as a sustainable alternative to plastic packaging **(Stoica et al. 2024; Siddiqui et al. 2024; Jha et al. 2024)**. Solution-cast cellulose films involve complex processes and are hard to mass-produce **(P. Grzybek et al. 2024)**. By contrast, wood-pulp cellulose paper fabricated by traditional papermaking is low-cost and easily scalable for industrial use. However, neat cellulose paper fails to meet fruit preservation demands. Low thermal conductivity leads to unstable packaging microenvironments, absence of active groups removes anti-oxidant/antibacterial ability, and porous structures weaken barrier properties, collectively accelerating fruit spoilage under ambient conditions **(Mohamed et al. 2025; Kolbl Repinc et al. 2024; Kathuria and Zhang 2022; Mujtaba et al. 2022; Sangroniz et al. 2019)**.

To overcome these limitations, proanthocyanidins (PACI) and hexagonal boron

nitride (*h*-BN) have been separately utilized as functional modifiers for cellulose substrates **(I. Stepina et al. 2023)**. Pure PACI can endow cellulose paper with antioxidant, antibacterial, UV-blocking and barrier improvements **(Santos-Buelga and Scalbert 2000; Rue et al. 2017; Nie et al. 2023; A.Yu et al. 2025; Tang et al. 2020; Rauf et al. 2019; Z. Xu et al. 2012; Y.Yu et al. 2026)**. While free PACI self-aggregates in pulp, resulting in uneven distribution and easy leaching in humid conditions. Besides, PACI is incapable of enhancing thermal conductivity, so packaging internal temperature and humidity remain unregulated. Pristine *h*-BN delivers excellent thermal conductivity, physical UV shielding and barrier properties, yet severe lamellar stacking and weak van der Waals interfacial adhesion with cellulose bring on serious filler agglomeration and deteriorated mechanical/barrier properties **(Shams et al. 2023; Zhang et al. 2021; W. Liu et al. 2019; Qadir et al. 2021; Rasul et al. 2021; R. Wang et al. 2023; Santos et al. 2021; Kostoglou et al. 2014; Kıvanç et al. 2018; M. Liu and Wang 2026)**. Up to now, no studies have realized the organic-inorganic covalent integration of PACI and *h*-BN to solve the above dual aggregation problems, and there lacks a green, scalable fabrication route to prepare multifunctional cellulose packaging for fresh fruit preservation **(Y. Yu et al. 2022; Roudi et al. 2024; Wu et al. 2022)**.

We hypothesize that PACI-modified boron nitride nanosheets can simultaneously suppress PACI self-aggregation and *h*-BN restacking. The resulting *h*-BN-g-PACI hybrid, when uniformly dispersed in a cellulose matrix, is expected to impart enhanced antioxidant activity, thermal conductivity, barrier properties, and

UV-shielding performance, thereby favouring long-term fruit preservation. The key challenges to be addressed for this hypothesis are: (i) how to efficiently graft PACI onto the surface of exfoliated h-BN sheets, and (ii) how to achieve a homogeneous dispersion of *h*-BN-g-PACI within the cellulose matrix.

In this work, a simple, solvent-free mechanochemical ball-milling exfoliation strategy is adopted to synthesise the *h*-BN-g-PACI hybrid filler, which effectively resolves the grafting issue. Subsequently, environmentally benign conventional papermaking techniques are employed to prepare cellulose/*h*-BN-g-PACI composite packaging paper. The abundant phenolic hydroxyl groups on *h*-BN-g-PACI form multiple hydrogen bonds with cellulose fibres, optimising interfacial compatibility and promoting uniform filler dispersion, thus overcoming the dispersion difficulty. Importantly, the entire preparation process avoids toxic organic solvents, making it environmentally sustainable and scalable. The microstructure, elemental distribution, crystal structure and interfacial chemical interactions of as-prepared fillers were systematically characterized by SEM, EDS, XRD, FTIR, XPS and TGA. A series of macroscopic performances including mechanical strength, thermal conductivity, UV shielding, surface hydrophobicity and water vapor barrier were measured with different filler loadings, and DPPH assay was carried out to evaluate antioxidant capacity. Furthermore, cherry tomato ambient storage experiments were conducted to verify the practical fresh-keeping efficacy of composite paper. This work aims to clarify the structure-performance relationship of *h*-BN-g-PACI reinforced cellulose paper, and provide a green, scalable fabrication strategy for multifunctional biomass

fruit packaging materials.

Experimental section

Materials

The softwood pulp was purchased from Sichuan Fengsheng Paper-making Co. Ltd., which possessed cellulose $(C_6H_{10}O_5)_n$ with an average degree of polymerization (DP) of approximately 1200 (based on Copper ethylenediamine solution method, according to the Chinese National Standards (GB/T 5888-2016) and ISO standards (ISO 5351:2010)) and a calculated average relative molecular weight of about 2×10^5 g/mol (**detailed method is in Supporting Information)**. Cellulose pulp suspension was prepared from softwood pulp (freeness: 80 °SR; average fiber length: 0.848 mm; average width: 27.4 μm; **detailed preparation is in Supporting Information**). The hexagonal boron nitride (*h*-BN) used in this work was purchased from Macklin Reagent Inc. (99.9 % purity, particle size range 1-2 μm, molecular weight 24.82 g/mol). Proanthocyanidins (PACI) (> 95 % purity, CAS 4852-22-6) purchased from Macklin Reagent Inc. Sinopharm Chemical Reagent Co. supplied the absolute ethanol (99 % purity, Analytical Reagent). Deionized (DI) water was prepared in Laboratory.

Preparation of *h*-BN-g-PACI

h-BN-g-PACI powder was fabricated via mechanochemical grafting. Briefly, 2 g *h*-BN and 10 g PACI were loaded into a PTFE jar with mixed-size zirconia balls, followed by ball milling at 450 rpm for 12 h. This condition enables exfoliation of bulk *h*-BN into few-layer sheets and creates active edge/defect sites for homogeneous

mixing with PACI, while preventing severe degradation of organic components and excessive sheet fragmentation **(C. Gautam and S. Chelliah 2021)**. The milled powder was purified by repeated DI water washing and centrifugation (9000 rpm, 10 min per cycle, 16 cycles) to remove unreacted free PACI until the supernatant became nearly colorless. The harvested sediment was re-dispersed in DI water and exfoliated by probe sonication (1800 W, 1 h). The primary dispersion was equally divided, diluted with DI water and further sonicated (1800 W, 1 h) to obtain a stable, homogeneous aqueous *h*-BN-g-PACI suspension for composite fabrication **(Fig. 1)**.

Preparation of cellulose/*h*-BN-g-PACI composite papers

Pure cellulose paper and cellulose/*h*-BN-g-PACI composite papers were fabricated by incorporating *h*-BN-g-PACI sheets into a cellulose matrix at varied mass fractions. Cellulose suspension was prepared from softwood pulp (freeness: 80 °SR; average fiber length: 0.848 mm; average width: 27.4 μm; **see Supporting Information for detailed preparation**). Neat cellulose paper (0 wt% *h*-BN-g-PACI) was manufactured under identical conditions without fillers. Composite papers with three *h*-BN-g-PACI loadings (20 wt%, 40 wt% and 60 wt%) were prepared accordingly. All suspensions were vacuum-filtered with a standard sheet former to obtain wet sheets with homogeneous thickness and fiber distribution **(Fig. 1)**. Subsequently, the wet sheets were pressed and dried for 4 min on a paper machine to remove excess water and consolidate the fiber network.



Fig. 1 Schematic illustration showing the entire fabrication process of *h*-BN-g-PACI and cellulose/*h*-BN-g-PACI composite papers, including ball milling, purification, freeze-drying and paper formation.

Instrumental characterization

Scanning Electron Microscopy (SEM) and Energy Dispersive Spectroscopy (EDS): The surface morphology and elemental distribution of *h*-BN-g-PACI were characterized via SEM-EDS (VEGA 3 SBH, Tescan, Czech Republic) under high vacuum at 10-20 kV.

Particle size: The Particle size distribution of *h*-BN-g-PACI aqueous dispersion was determined by a Bettersize 3000 Plus laser diffraction analyzer (Baite, China); samples were diluted with DI water and sonicated for 1 h prior to testing to guarantee homogeneity.

X-ray Diffraction (XRD): XRD patterns of *h*-BN, PACI and *h*-BN-g-PACI powders

were collected on a D8 Advance diffractometer (Bruker AXS, Germany) with Ni-filtered Cu Kα radiation (40 kV, 40 mA), scanning from 3 ° to 60 ° at 4 °/min.

Fourier Transform Infrared Spectroscopy (FT-IR): FT-IR spectra of all powders and cellulose-based papers were recorded on a Nicolet Nexus 470 spectrometer (Thermo Electric, USA), with a resolution of 4 cm^{-1} and 64 accumulated scans.

X-ray Photoelectron Spectroscopy (XPS): XPS analysis of *h*-BN-g-PACI was performed on a Kratos AXIS Ultra DLD instrument (Manchester, UK) equipped with a monochromatic Al Kα X-ray source.

Thermogravimetric Analysis (TGA/DTG): TGA/DTG measurements were carried out on a STA449F3 thermal analyzer (NETZSCH, Germany) under nitrogen atmosphere from 40 °C to 600 °C at a heating rate of 10 °C/min.

Thermal conductivity: The room-temperature thermal conductivity of paper samples was tested using a TPS 2200 thermal constant analyzer (Hot Disk AB, Sweden), and surface temperature variation was monitored by a GR-STMS-1901 system.

Tensile test : Tensile mechanical performances of neat cellulose and composite papers were measured on an AI-7000-NGD universal tester (Goodtechwill, China) at a stretching rate of 5 mm/min; each sample (3 cm × 2 cm) was tested in triplicate to obtain average values.

The thermal conductivity and mechanical performance tests were conducted in a constant temperature and humidity laboratory, with temperature and humidity as standard conditions, that is, a temperature of 25 degrees Celsius and a relative humidity of 50%.

UV-Vis Transmission: UV–Vis-NIR reflectance spectra (200–800 nm) of paper specimens were acquired on an Agilent Cary 5000 spectrophotometer (Agilent, USA) fitted with an integrating sphere after baseline correction. Water contact angle was measured on an OCA20 goniometer (Dataphysics, Germany) and average values with standard deviations were calculated via the tangent method at multiple positions on each sample.

The antioxidant property: DPPH radical scavenging assay was applied to assess the antioxidant capacity of *h*-BN-g-PACI according to a reported procedure **(Gerasimova et al. 2022)**. Fresh 0.2 mM methanolic DPPH solution was mixed equally with sample dispersion, followed by dark incubation at 37 °C for 30 min. The absorbance at 517 nm was recorded, and radical scavenging efficiency was calculated using **Eq. (1)**.

$$\textbf{(\%)}\ \boldsymbol{Scavenging} = \left(\frac{A_C - A_S}{A_C}\right) \times \mathbf{100} \qquad \textbf{(1)}$$

With A_C is the absorbance of the test control and the A_S is absorbance of the *h*-BN-g-PACI.

Water vapor permeability (WVP): WVP of all paper samples (≥Φ74 mm, thickness ≤3 mm) was measured via the gravimetric cup method at 23 °C and 50 % relative humidity. The water vapor transmission rate (WVTR, $g \cdot m^{-2} \cdot day^{-1}$) was converted to water vapor permeability (WVP×$10^3 g \cdot \mu m \cdot m^{-2} \cdot day^{-1} \cdot KPa^{-1}$) using **Eq. (2) (Cazón et al. 2022)**, incorporating sample thickness and water vapor pressure difference across the membrane.

$$\boldsymbol{WVP} = \frac{\boldsymbol{WVTR} \times \boldsymbol{d}}{\boldsymbol{\Delta P_S}} \qquad \textbf{(2)}$$

Where d is the sample thickness, and ΔP_S is the water vapor pressure difference across the sample, at 23 °C.

Results and Discussion

Characterization of *h*-BN-g-PACI

The SEM images, particle size distribution of *h*-BN-g-PACI are shown in **Fig. 2**, as well as nitrogen adsorption-desorption isotherms and corresponding pore size distributions.

SEM micrographs **(Fig. 2A-C)** reveal that *h*-BN-g-PACI maintains the characteristic two-dimensional sheet structure of pristine *h*-BN after mechanical exfoliation and PACI grafting. The sheet surfaces become rough and are uniformly covered by amorphous organic coatings, and the sheet edges are passivated relative to neat *h*-BN. Noticeable stacking and agglomeration of sheets are observed, originating from strong hydrogen bonding between PACI chains and ice crystal squeezing during freeze-drying of the aqueous dispersion. No large aggregates of free PACI can be found, verifying the efficient purification after the grafting reaction. The particle size distribution **(Fig. 2D)** shows a D50 of 0.84 μm with a span of ~1.4, demonstrating the predominance of submicron particles and further confirming the disaggregation of bulk *h*-BN **(Bunpheng et al. 2025; Li et al. 2021)**.

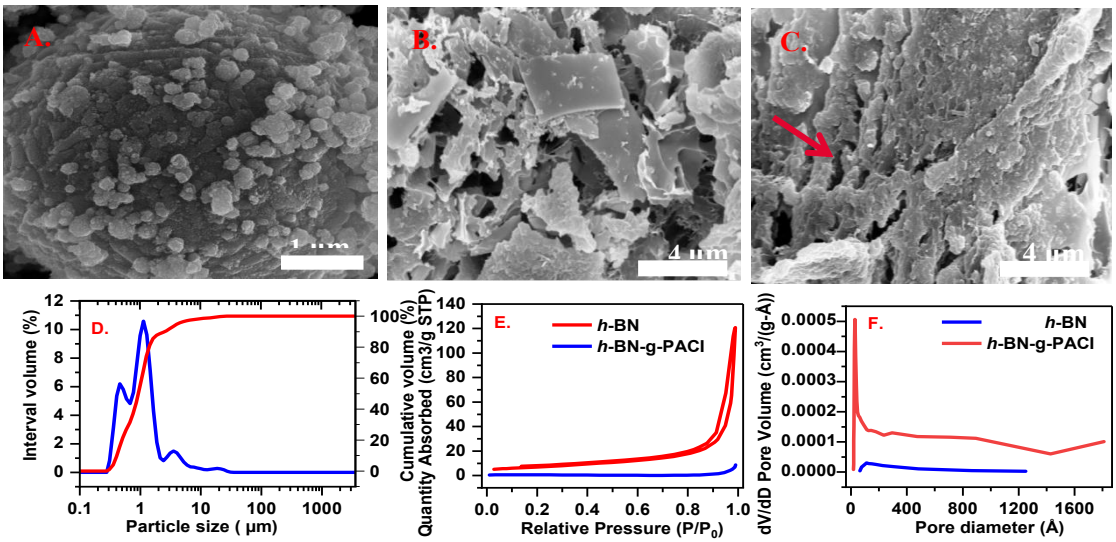


Fig. 2 SEM images of (A) Pristine *h*-BN at 500 nm, and (B), (C) *h*-BN-g-PACI at 4 μm. (D) Particle size distribution of *h*-BN-g-PACI dispersion, (E) N_2 adsorption-desorption curves and (F) the pore size distributions of *h*-BN and *h*-BN-g-PACI powders.

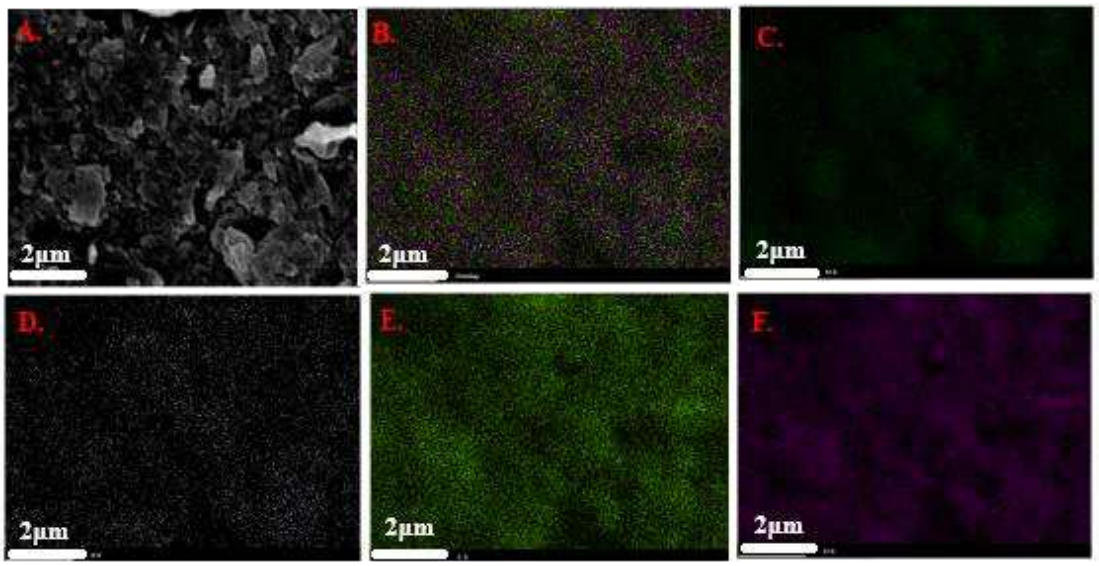
The Type IV isotherms with H3-type hysteresis loops (**Fig. 2E**) demonstrate the presence of mesopores and macropores in both pristine *h*-BN and *h*-BN-g-PACI powders, which is consistent with their pore size distribution results in **Fig. 2F**. These hierarchical pores mainly originate from sheet stacking, edge defects, and inter-particle voids. The anchored PACI molecules act as intersheet adhesives that tightly connect adjacent BN layers and partially fill interlayer gaps. Consequently, most slit pores produced by mechanical exfoliation are blocked by organic coatings and sheet aggregates, restricting nitrogen adsorption primarily to the external surface of the agglomerated powders. This structural variation explains why *h*-BN-g-PACI has a significantly lower specific surface area (1.309 m^2/g) than pristine bulk *h*-BN

245 (24.4733 m^2/g) **(Itskou et al. 2023; Li et al. 2013)**.

246

247 Combined evidence from SEM morphology, particle size distribution, and
248 Brunauer-Emmett-Teller (BET) results prove that PACI-assisted mechanical ball
249 milling successfully exfoliated bulk *h*-BN into few-layer sheets.

250 EDS elemental mapping of *h*-BN-g-PACI is shown in **Fig. 3**. The elements boron,
251 nitrogen, carbon, and oxygen are homogeneously distributed, with 8, 20, 32 and 39 %,
252 respectively. The B and N content is relatively low, while signals for C and O are
253 dominant, which suggests that the surface of *h*-BN is covered densely grafted by the
254 PACI that is rich in carbon and oxygen-containing functional groups **(Yang et al.**
255 **2023; Zhou et al. 2023)**. The uniform overlap of C and O signals with the underlying
256 B and N distribution **(Fig. 3B)** validates that PACI is not merely physically mixed
257 with *h*-BN, but is intimately and homogeneously grafted onto the sheet surface. This
258 observation is in accordance with the continuous organic coating of the sheets seen in
259 the SEM image.



260

Fig. 3 SEM image and EDS elemental mapping of *h*-BN-g-PACI powder: (A) SEM micrograph, (B) overlay elemental map showing B, C, N, and O distribution, (C) N mapping, (D) B mapping, (E) C mapping, and (F) O mapping.

In order to further verify the successful functionalization of *h*-BN with PACI and further corroborates the SEM and EDS analysis, the pristine *h*-BN, pure PACI and the functionalized *h*-BN-g-PACI powder were characterized by XRD, FTIR and XPS measurements and the results are evaluated collectively as shown in **Fig. 4**.

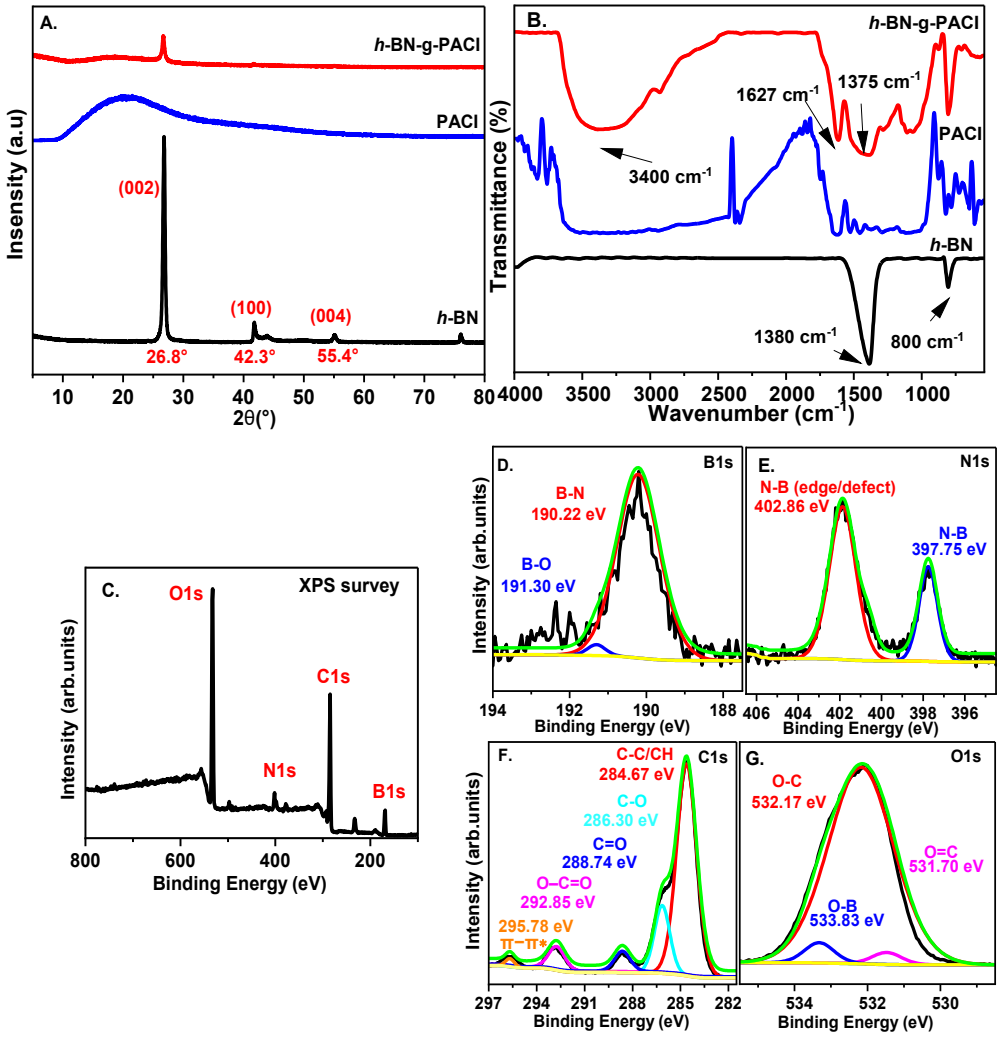


Fig. 4 The structure and elemental analysis of *h*-BN, PACI and *h*-BN-g-PACI, (A) XRD patterns and (B) FTIR spectra of pure *h*-BN, pure PACI, and *h*-BN-g-PACI.

XPS analysis of *h*-BN-g-PACI: (C) full survey spectrum, and high-resolution deconvoluted spectra of (D) B 1s, (E) N 1s, (F) C 1s, and (G) O 1s.

As displayed in the XRD patterns (**Fig. 4A**), pristine *h*-BN presents three distinct diffraction peaks at 2θ = 26.8 °, 42.3 °, and 55.4 °, which are assigned to the (002), (100), and (004) crystal planes of hexagonal boron nitride, respectively, demonstrating its well-defined crystalline structure **(Tian et al. 2017; Wang et al. 2021)**. Pure PACI exhibits only a broad amorphous diffraction halo ranging from 20 ° to 25 ° without obvious crystalline peaks, which is typical for amorphous polyphenol polymers **(Biao et al. 2018)**. For *h*-BN-g-PACI, the characteristic diffraction peaks of *h*-BN are completely preserved without peak shifting or emerging impurity signals, while a weak amorphous background correlated with PACI is observed. These findings indicate that the mechanochemical grafting treatment only modifies the *h*-BN surface and does not damage its intrinsic layered crystal structure. Notably, the (002) diffraction peak of *h*-BN-g-PACI shows obvious broadening and decreased intensity compared with pristine *h*-BN. This phenomenon suggests a reduced stacking degree along the c-axis and diminished lateral crystallite size, further explaining the successful exfoliation of multilayer sheets into few-layer sheets during ball milling.

As illustrated in the FTIR spectra (**Fig. 4B**), pristine *h*-BN presents two typical absorption bands: a strong B-N in-plane stretching vibration at 1380 cm^{-1} and a B-N-B out-of-plane bending vibration at 800 cm^{-1}**(Peng et al. 2023; Hung et al. 2014; Tian et al. 2025)**. Pure PACI displays a broad O-H stretching band centered at

294 approximately 3500 cm^{-1}, aliphatic C-H stretching vibrations near 2900 cm^{-1}, and
295 multiple characteristic peaks assigned to aromatic C=C, C=O, and C–O stretching
296 modes within the fingerprint region of 1000–1600 cm^{-1}, which is attributed to
297 abundant phenolic structures and extensive intermolecular hydrogen bonding in PACI
298 molecules **(Li et al. 2023; Grasel et al. 2016)**.

299 In comparison, *h*-BN-g-PACI simultaneously displays the intrinsic B–N
300 characteristic bands of *h*-BN and typical organic absorption signals of PACI,
301 confirming the successful introduction of PACI onto the *h*-BN surface. After grafting,
302 the severe self-aggregation of PACI is effectively inhibited, resulting in resolved and
303 distinguishable absorption peaks. Specifically, new characteristic humps appear at
304 1627 cm^{-1} (aromatic C=C stretching) and 1375 cm^{-1} (coupled vibrations of
305 phenolic O–H in-plane bending and aromatic C–O stretching). Both peaks shift
306 toward lower wavenumbers relative to pure PACI. Meanwhile, the broad O–H
307 stretching intensity of *h*-BN-g-PACI is remarkably reduced. These spectral variations
308 strongly verify the formation of covalent linkages between the phenolic hydroxyl
309 groups of PACI and the exposed boron active sites of *h*-BN during mechanochemical
310 ball milling.

311 XPS measurements were performed to clarify the surface chemical states of
312 *h*-BN-g-PACI and reveal the interfacial interaction between *h*-BN and grafted PACI.
313 The full survey spectrum **(Fig. 4C)** displays distinct B 1s, N 1s, C 1s, and O 1s signals,
314 in which the emerging C and O elements confirm the successful immobilization of
315 PACI on the *h*-BN surface.

316 The high-resolution B 1s spectrum **(Fig. 4D)** is deconvoluted into two
317 characteristic peaks at 190.22 eV and 191.30 eV, corresponding to intrinsic B–N
318 bonds of the *h*-BN lattice and newly formed B–O covalent bonds, respectively. The O
319 1s spectrum **(Fig. 4G)** further presents a typical B–O signal at 533.83 eV, mutually
320 verifying the generation of B–O bonding. Mechanical ball milling creates numerous
321 unsaturated edge B active sites on exfoliated sheets, which readily react with phenolic
322 hydroxyl groups of PACI under mechanochemical activation, thereby constructing
323 stable B–O–C covalent interfacial linkages **(Mannan et al. 2008)**. Such covalent
324 bonding serves as the dominant grafting mode between *h*-BN and PACI.

325 The high-resolution N 1s spectrum **(Fig. 4E)** is fitted into two peaks. The peak
326 at 397.75 eV originates from lattice N–B bonds of pristine *h*-BN, while the peak at
327 402.86 eV corresponds to defective edge N–B sites induced by mechanical exfoliation.
328 The high-resolution C 1s spectrum **(Fig. 4F)** is decomposed into five individual
329 components at 284.67 eV (C–C/C–H), 286.30 eV (C–O), 288.74 eV (C=O), 292.85
330 eV (O–C=O), and 295.78 eV ($\pi \rightarrow \pi^*$ shake-up satellite of aromatic carbon), consistent
331 with the typical carbon-containing functional groups of polyphenol structures **(Chen**
332 **et al. 2019; Guerra and McNally 2019; Dee et al. 2023)**.

333 Overall, XPS results systematically demonstrate that PACI is covalently grafted
334 onto the *h*-BN surface via B–O–C linkages. Combined with repeated solvent washing
335 and subsequent TGA characterization, the stable retention of PACI moieties further
336 excludes weak physical adsorption or reversible hydrogen-bond interaction,
337 confirming the formation of robust covalent grafting structure.

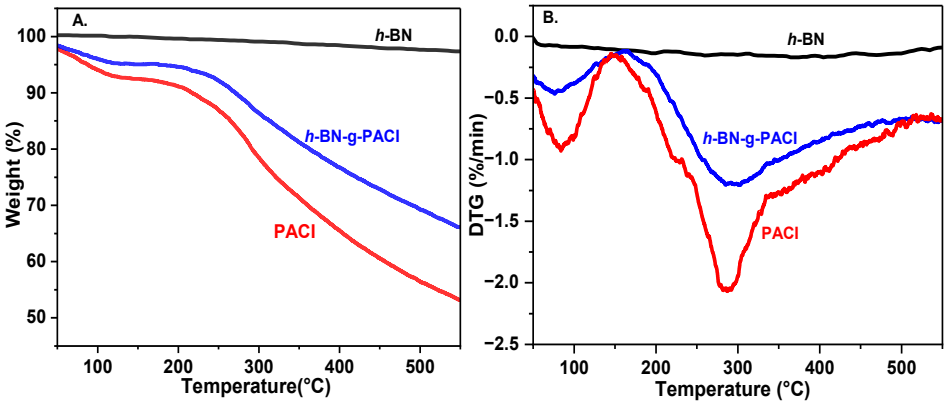


Fig. 5 Thermal stability analysis of *h*-BN, PACI, and *h*-BN-g-PACI under nitrogen atmosphere, (A) Thermogravimetric (TGA) and (B) differential thermogravimetric (DTG).

As revealed by the TGA curves (**Fig. 5A**), pristine *h*-BN exhibits nearly negligible weight loss up to 550 °C, demonstrating its outstanding thermal stability under the tested conditions **(Kostoglou et al. 2014; Cai et al. 2026)**. In contrast, pure PACI undergoes substantial thermal degradation, with a total weight loss of approximately 47 % and a residual char yield of 53 % at 550 °C, due to the thermal decomposition and partial carbonization of organic polyphenol segments **(Rauf et al. 2019)**. The corresponding DTG profile of pure PACI **(Fig. 5B)** displays a dominant decomposition peak centered near 300 °C, representing the maximum thermal degradation rate of PACI. For *h*-BN-g-PACI, the total weight loss reaches approximately 32 % at 550 °C, falling between the values of pristine *h*-BN and pure PACI. Compared with neat PACI, the DTG peak of *h*-BN-g-PACI becomes weaker and slightly shifts, further verifying the successful grafting of PACI on the *h*-BN surface. The suppressed decomposition rate indicates that the covalent interfacial interaction effectively restricts the thermal cleavage of PACI molecular chains,

thereby improving the thermal stability of grafted organic components.

By calibrating the residual mass proportion of pure PACI, the effective grafting content of PACI anchored on *h*-BN sheets is calculated to be 66.7 %. This quantitative result further confirms the successful introduction and high loading of organic PACI components onto the inorganic *h*-BN substrate via mechanochemical grafting.

Morphology of cellulose/*h*-BN-g-PACI composite papers

Fluorescence microscopy and 3D digital microscopy were employed to investigate the filler dispersion and surface microstructure of neat cellulose paper and cellulose/*h*-BN-g-PACI composite papers. **Fig. 6**. displays fluorescence micrographs (A–D) and 3D surface morphologies (E–H) of samples with varying *h*-BN-g-PACI loadings: 0 wt%, 20 wt%, 40 wt%, and 60 wt%. Nearly no fluorescent signal is observed for pure cellulose paper.

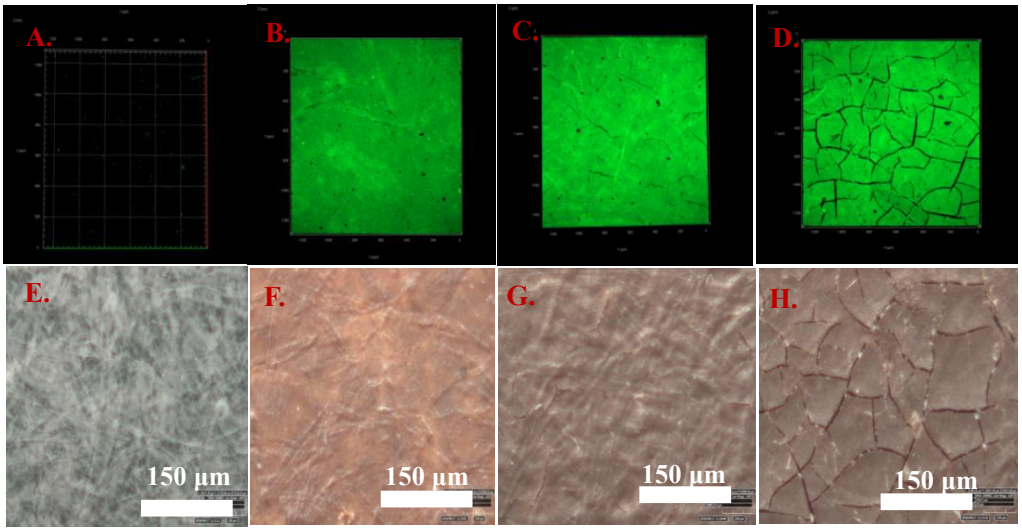


Fig. 6 Fluorescence images (A–D) and 3D digital microscope photographs (E–H) of neat cellulose paper and cellulose/h-BN-g-PACI composite papers with different filler loadings. (A, E) 0 wt%; (B, F) 20 wt%; (C, G) 40 wt%; (D, H) 60 wt%.

Almost no fluorescent signal can be detected on neat cellulose paper. At low and moderate filler contents (20 wt% and 40 wt%), homogeneous green fluorescence distribution demonstrates the uniform dispersion of *h*-BN-g-PACI within the cellulose matrix, accompanied by intact and crack-free paper surfaces. In contrast, obvious filler aggregation and distinct surface cracks emerge when the filler loading increases to 60 wt%, indicating deteriorated dispersion uniformity at excessive doping levels.

Further SEM characterization reveals the fine surface texture and internal cross-sectional structure **(Fig. 7)**. Neat cellulose paper possesses a typical densely interwoven fiber network structure **(Xu et al. 2020)**. At appropriate loadings, *h*-BN-g-PACI sheets are uniformly embedded among cellulose fibers, forming a well-integrated composite structure. However, excessive incorporation (60 wt%) leads to severe filler agglomeration and generates numerous interfacial voids and structural defects within the cellulose matrix.

FT-IR and XRD Analysis of cellulose/*h*-BN-g-PACI composite Papers

The FT-IR and XRD results shown in the **Fig. S3** support this structural change observed in SEM results. According to the XRD patterns **(Fig. S3(A))**, pure cellulose paper presents its usual crystalline peaks at 15° and 22° **(Park et al. 2010)**. With the increase in *h*-BN-g-PACI loading, a sharp intense peak appears near 26°, corresponding to the characteristic (002) reflection of h-BN. Its intensity increased with the filler content confirming the gradual development of the BNs phase. The

corresponding FT-IR spectra **(Fig. S3(B))** display the pure cellulose spectrum with two significant absorption bands around 3350 cm^{-1}(O–H stretching) and 1350 cm^{-1}**(Atykyan et al. 2020; Oh et al. 2005)**, while the composite samples include new bands at about 1348 cm^{-1} and 900 cm^{-1}, which typically correspond to B–N stretching and B–N–B bending related to boron nitride sheets.

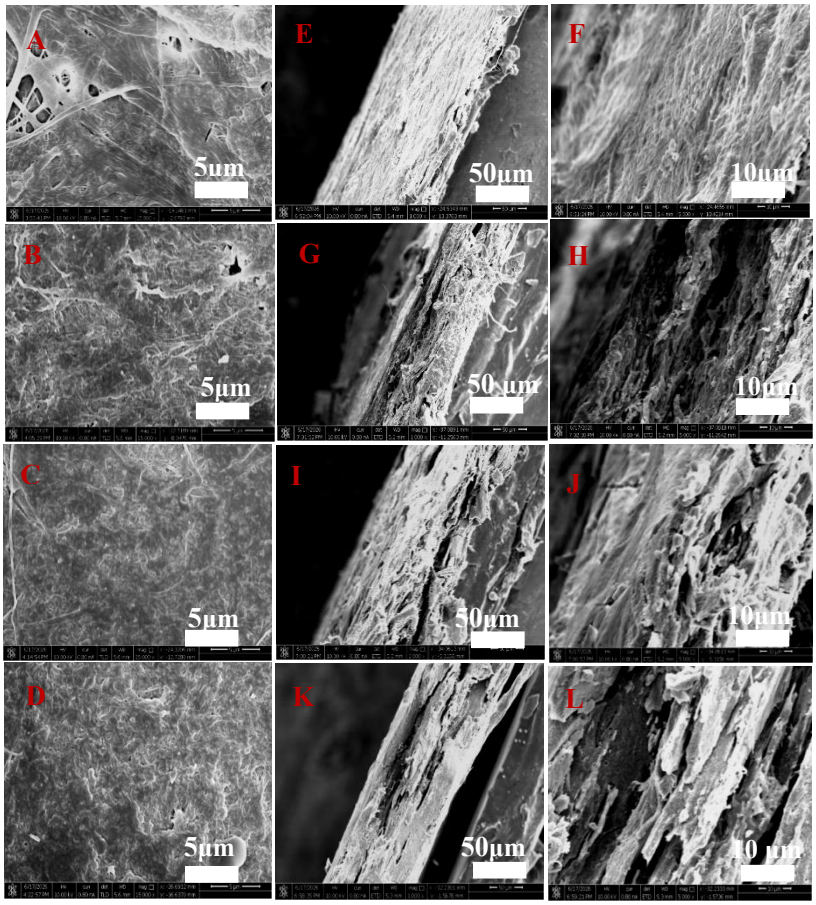


Fig. 7 SEM micrographs of neat cellulose paper and cellulose/*h*-BN-g-PACI composite papers with various filler contents. (A–D) Surface morphology; (E, G, I, K) cross-section morphology at low magnification; (F, H, J, L) cross-section morphology at high magnification. (A, E, F) 0 wt%; (B, G, H) 20 wt%; (C, I, J) 40 wt%; (D, K, L) 60 wt%.

Mechanical and thermal conductive properties of composite papers

The above microstructural evolution directly governs the macroscopic mechanical and thermal performances of the resultant paper samples **(Fig. 8)**. Neat cellulose paper presents a tensile strength of 30 MPa, a Young's modulus of 15 MPa, and a breaking strain of 7.6 % **(Santmarti et al. 2020; Jo et al. 2021; Dislaire et al. 2021)**. After the incorporation of *h*-BN-g-PACI, the mechanical performances are significantly improved, with the optimal tensile strength (70 MPa) and Young's modulus (26 MPa) achieved at a filler loading of 40 wt%. Such prominent mechanical reinforcement is resulted from good dispersion of *h*-BN-g-PACI in the cellulose matrix, strong matrix–filler adhesion and efficient interfacial stress transfer, which are facilitated by abundant hydrogen-bonding interactions between the PACI functional groups and cellulose chains.

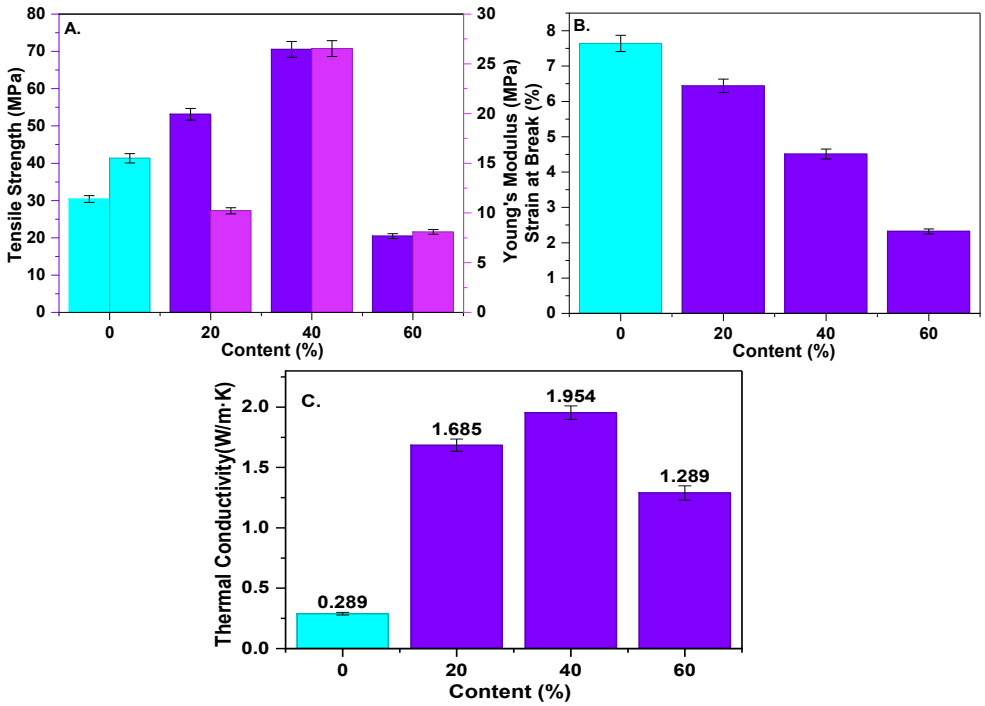


Fig. 8 Mechanical and thermal conductive properties of neat cellulose paper and cellulose/*h*-BN-g-PACI composite papers with different *h*-BN-g-PACI loadings. (A) Tensile strength, (B) strain at break, and (C) thermal conductivity.

Nevertheless, the breaking strain decreases gradually with increasing *h*-BN-g-PACI content. The rigid inorganic BN sheets restrict the slippage and movement of cellulose molecular chains, thereby reducing the ductility of the composite papers. Obviously, excessive filler incorporation (60 wt%) introduces substantial interfacial voids and aggregated defects, which act as stress-concentration sites under external loading. Consequently, the tensile strength and Young's modulus sharply decline to 20 MPa and 8 MPa, respectively.

Similar variation trends are observed for thermal conductivity. Neat cellulose paper exhibits a low thermal conductivity of 0.289 W/m·K **(Apostolopoulou-Kalkavoura et al. 2020; Antlauf et al. 2021; Rbihi et al. 2019)**. With increasing *h*-BN-g-PACI loading, the thermal conductivity of composite paper gradually increases and reaches a maximum value of 1.954 W/m·K at 40 wt%, representing a 5.76-fold enhancement compared with pure cellulose paper. At this optimal filler content, uniformly dispersed *h*-BN-g-PACI fillers construct efficient and continuous thermal conduction networks within the cellulose matrix, thereby significantly promoting phonon transmission. However, further increasing the filler loading to 60 wt% induces severe sheet aggregation, surface cracks, and abundant interfacial voids. These structural defects strongly intensify phonon scattering and disrupt the thermally conductive pathways, ultimately leading to a declined thermal conductivity. The deteriorated mechanical and thermal performances at 60 wt% are highly agreement with the microscopic observations in **Figs. 6** and **7**, testifying that excessive filler incorporation inevitably causes structural inhomogeneity and defect

generation, which fundamentally degrade the comprehensive properties of composite papers.

Antioxidant activity, UV-Shielding performance, barrier property and surface wettability of composite papers

Owing to the abundant phenolic hydroxyl groups in PACI, the functionalized sheets can donate hydrogen atoms or electrons to neutralize free radicals. Accordingly, PACI-modified *h*-BN sheets serve as an efficient radical scavenger, similar to previously reported biomass-derived antioxidant fillers **(Cao et al. 2018; Balasubramaniam et al. 2021)**. The measured DPPH radical scavenging efficiency of *h*-BN-g-PACI reaches 79.4 %, demonstrating that surface grafted PACI endows inert *h*-BN with excellent antioxidant activity.

UV-Vis reflectance spectra **(Fig. 9A)** further illustrate the optical shielding performance of the cellulose/*h*-BN-g-PACI composite papers. Neat cellulose paper displays strong reflectance across the ultraviolet range. By contrast, the incorporation of *h*-BN-g-PACI significantly reduces the reflectance intensity within 200–600 nm, and the UV-blocking ability is gradually enhanced with increasing filler loading. Combined with the superior radical-scavenging property of *h*-BN-g-PACI, the outstanding UV-shielding capability enables the composite papers to effectively inhibit light-triggered lipid oxidation, showing great potential for fresh fruit packaging applications.

As presented in **Fig. 9B**, the water contact angle (WCA) increases monotonically

with increasing *h*-BN-g-PACI loading, rising from 63.21 ° for neat cellulose paper to 78.33 ° for the composite paper with 60 wt% filler content. The inherent hydrophobic nature of *h*-BN, together with the increased surface micro-roughness induced by nanofiller incorporation, synergistically improves the surface hydrophobicity of the composite papers **(Zang et al. 2026; Alebachew et al. 2025)**. Accordingly, the water vapor permeability (WVP) drops sharply with increasing *h*-BN-g-PACI content **(Fig. 9C)**. Pure cellulose paper displays a high WVP of 13.87×10^{3} $g\cdot$ μm$\cdot$ $m^{-2}\cdot$ $day^{-1}\cdot KPa^{-1}$, while the values decrease to 9.3×10^{3}, and 8.1×10^{3} $g\cdot$ μm$\cdot$ $m^{-2}\cdot$ $day^{-1}\cdot KPa^{-1}$ at filler loadings of 20 wt% and 40 wt%, respectively. The improved water barrier performance originates from two synergistic effects. On the one hand, the incorporation of hydrophobic *h*-BN-g-PACI reduces surface wettability and suppresses water vapor adsorption at the paper surface. On the other hand, the uniformly dispersed two-dimensional sheets create highly tortuous and prolonged diffusion pathways for water vapor molecules penetrating through the cellulose matrix **(Ayub et al. 2021; Zhang et al. 2026; Li et al. 2019)**. Nevertheless, excessive filler loading (60 wt%) induces severe aggregation and interfacial defects, which destroy the continuous barrier structure and consequently cause a slight rebound in WVP values, 8.1×10^{3} $g\cdot$ μm$\cdot$ $m^{-2}\cdot$ $day^{-1}\cdot KPa^{-1}$. Overall, the composite paper with the optimal 40 wt% *h*-BN-g-PACI loading exhibits outstanding comprehensive performances. Uniformly dispersed *h*-BN-g-PACI sheets construct continuous thermal conduction networks, significantly enhancing thermal conductivity and mechanical properties. Meanwhile, the combination of enhanced

surface hydrophobicity and tortuous diffusion pathways generated by two-dimensional sheets effectively suppresses water vapor penetration. Furthermore, the grafted PACI endows the composite paper with prominent UV-shielding capacity and efficient free radical scavenging activity. These multifunctional synergies enable the composite paper to achieve efficient heat dissipation, UV blocking, moisture barrier and free radical elimination simultaneously. These favorable characteristics are expected to retard food oxidative deterioration. Nevertheless, the practical preservation efficacy for fresh fruits remains to be verified by storage experiments, which will be systematically investigated in the following section.

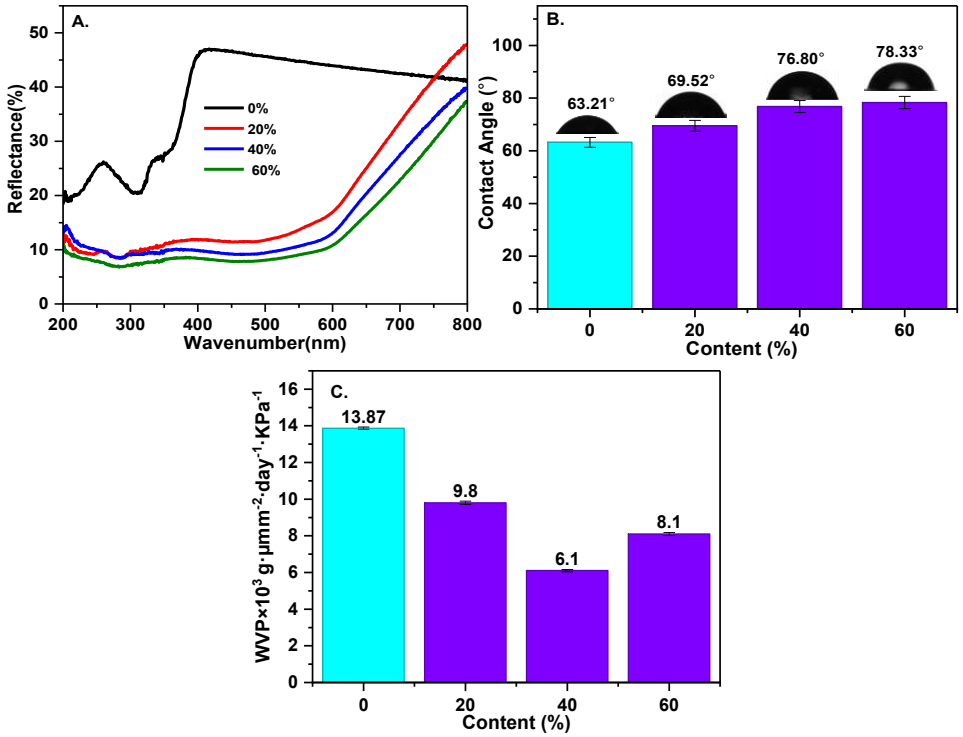


Fig. 9 Optical, wetting and vapor permission properties of cellulose-based composite papers with different *h*-BN-g-PACI filler loadings, (A) UV–Vis reflectance spectra, (B) water contact angle (WCA), and (C) water vapor permeability (WVP) .

519 **Preservation effect of cellulose/*h*-BN-g-PACI composite paper on cherry**
520 **tomatoes**

521 Digital photographs tracking the visual evolution of cherry tomatoes packaged
522 with different materials (uncovered blank control, commercial PP film packaging,
523 neat cellulose paper packaging, and cellulose/*h*-BN-g-PACI composite paper
524 packaging) were acquired to preliminarily assess the preservation performance under
525 ambient storage conditions **(Fig. 10)**.

526 Distinct differences in fruit appearance gradually appear with prolonged storage
527 time. After 10 days of storage, the blank control group suffers severe water loss,
528 surface shrinkage and fungal contamination. Extensive mold proliferation and tissue
529 decay are observed on cherry tomatoes from the blank group on day 24. Samples
530 packaged with neat cellulose paper also exhibit obvious shriveling and mildew growth.
531 Commercial PP films can mitigate water evaporation, whereas their poor gas
532 permeability tends to trigger undesirable anaerobic respiration of fruits. By
533 comparison, cherry tomatoes wrapped with cellulose/*h*-BN-g-PACI composite paper
534 retain intact surface morphology and achieve remarkable delay in rot and mildew
535 formation throughout the storage period.

536 The evolution of soluble solids content (Brix value) and weight loss rate of
537 cherry tomatoes during 14 days of ambient storage were further quantified, as shown
538 in **Fig. 11**.

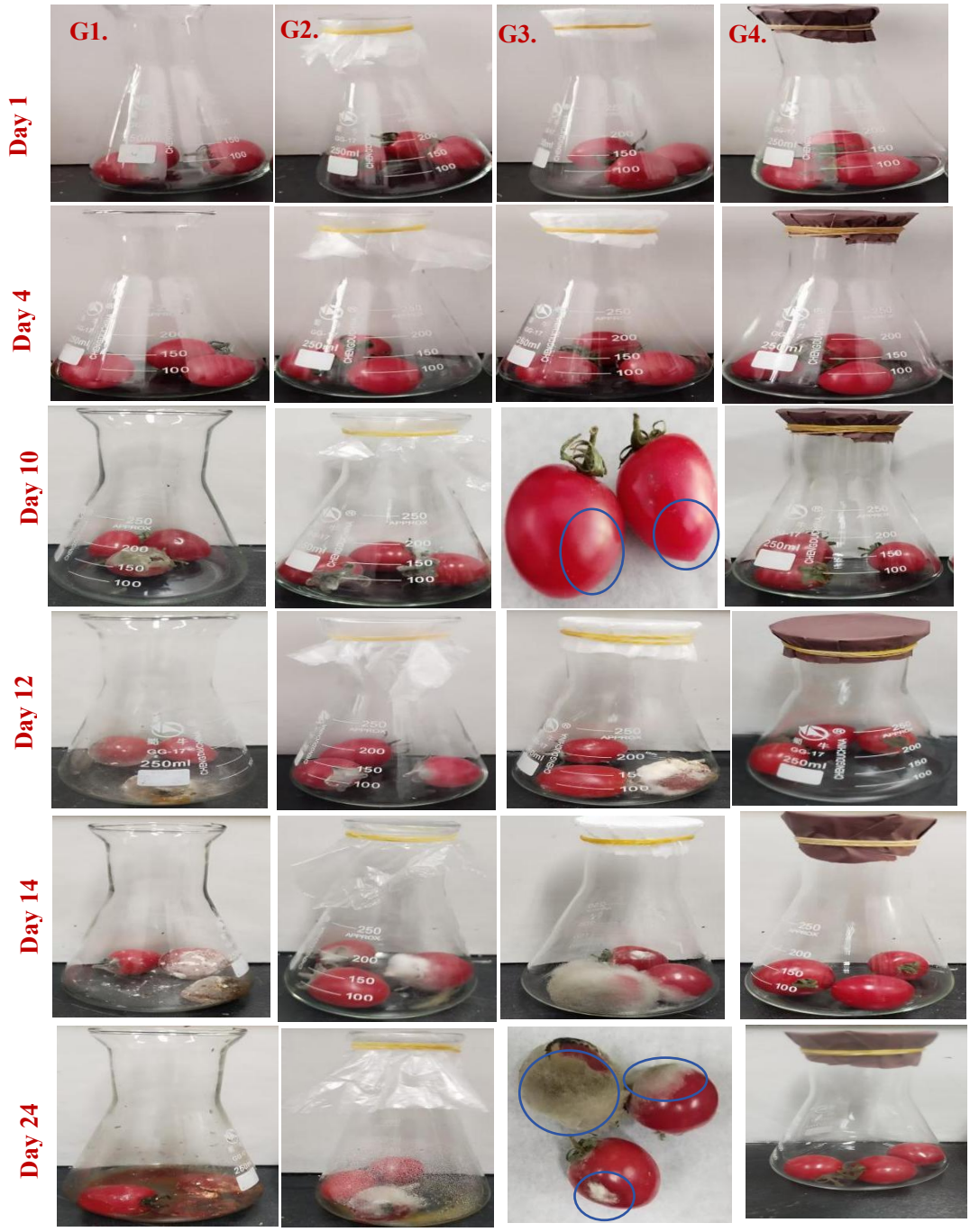


Fig. 10 Visual evaluation of tomato preservation/freshness over storage time using different packaging materials: (G1) Control (unpackaged), (G2) PP film, (G3) neat cellulose paper, and (G4) cellulose/*h*-BN-g-PACI composite paper.

Obvious differences in tomato weight loss and Brix value among all groups during the 14-day storage period are observed in **Fig.11**. The unpackaged control

group undergoes rapid water evaporation, resulting in the most serious weight loss and a sharp increase in soluble solids accompanied by accelerated ripening. Although PP film effectively inhibits water transpiration, its poor air permeability causes excessive condensation inside the package and accelerates fruit spoilage. Neat cellulose paper only provides limited water vapor barrier, so considerable weight loss and continuous rises in Brix still occurs. By contrast, the cellulose/*h*-BN-g-PACIcomposite paper with 40 wt% filler loading delivers the best preservation performance. Benefiting from the enhanced water vapor barrier and surface hydrophobicity, the outward diffusion of water from tomatoes is greatly restricted, which directly reduces fruit weight loss. Meanwhile, the excellent UV-shielding capacity blocks photooxidation, and the prominent radical scavenging activity restrains the accumulation of reactive free radicals; these two synergistically slows fruit senescence and keeps the increase of Brix within a low range. Moreover, the improved thermal conductivity makes the temperature inside the package more uniform and alleviates temperature fluctuations, which greatly reduces water vapor condensation on the inner wall of the packaging paper. Less condensation further suppresses moisture loss and avoids microbial corruption induced by local high humidity. Integrating favorable moisture barrier, UV shielding, antioxidant activity, together with homogeneous temperature regulation derived from good thermal conductivity, the multifunctional composite paper significantly delays tomato ripening and cuts down water loss, further confirming its great prospect as a sustainable active packaging material for fresh fruits.

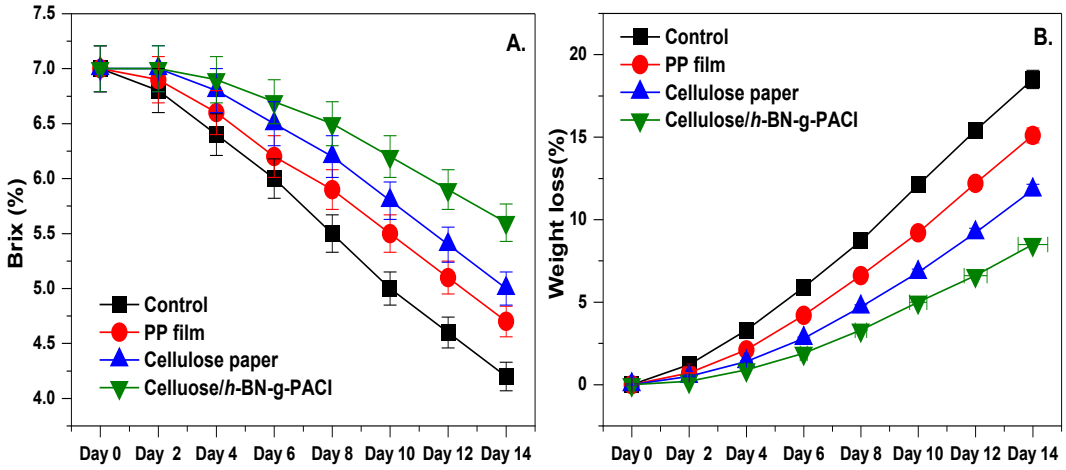


Fig. 11 Changes in (A) soluble solids content (Brix, %) and (B) weight loss ratio (%) of cherry tomatoes within a 14-day storage period. Four groups are set: Control (unpackaged cherry tomatoes), PP film packaging, neat cellulose paper packaging, and Cellulose/*h*-BN-g-PACI composite paper packaging.

Conclusion

This study verified our initial hypothesis that mechanochemical ball milling enables covalent grafting of PACI onto exfoliated *h*-BN sheets to simultaneously suppress the self-aggregation of PACI and stacking restacking of *h*-BN. The *h*-BN-g-PACI hybrid fillers were successfully synthesized via a solvent-free mechanochemical route, with a quantified PACI grafting ratio of 66.7 %. Multiple characterizations including XRD, FTIR, XPS, SEM and EDS collectively confirmed the formation of stable B–O–C covalent linkages between PACI and edge-defective *h*-BN, and the homogeneous distribution of B, N, C and O elements on *h*-BN-g-PACI sheets, which directly proves that the dual aggregation issue of organic polyphenols and inorganic *h*-BN sheets was well resolved as hypothesized.

The plentiful phenolic hydroxyl groups on grafted PACI generate abundant

584 hydrogen-bond interactions with cellulose fibers, greatly optimizing matrix-filler
585 interfacial compatibility and facilitating uniform filler dispersion at a moderate
586 loading of 40 wt%. At this optimal dosage, well-distributed *h*-BN-g-PACI constructs
587 continuous phonon conduction networks and efficient stress transfer channels,
588 delivering the maximum thermal conductivity of 1.954 W/m·K, tensile strength of 70
589 MPa. Benefiting from the two-dimensional sheet structure, tortuous water vapor
590 diffusion paths and enhanced surface hydrophobicity synergistically reduce water
591 vapor permeability. Besides, PACI immobilized on *h*-BN imparts excellent DPPH
592 radical scavenging ability and full-spectrum UV shielding performance to the
593 composite paper, realizing the integrated multifunctional performance we anticipated.
594 By contrast, excessive filler loading (60 wt%) triggers severe nanofiller
595 agglomeration, surface cracks and internal interfacial voids, resulting in aggravated
596 phonon scattering and stress concentration, which severely degrade mechanical,
597 thermal and barrier properties.

598 Ambient storage experiments of cherry tomatoes validate that the multifunctional
599 composite paper achieves superior fresh-keeping capacity through the synergy of heat
600 dissipation, moisture isolation, UV blocking and free radical elimination. Compared
601 with blank control, neat cellulose paper and commercial PP film, the 40 wt%
602 cellulose/*h*-BN-g-PACI packaging effectively slows fruit water loss, restricts the rise
603 of soluble solids, and delays mold proliferation and tissue deterioration.

604 The green, scalable mechanochemical grafting combined with traditional
605 papermaking strategy successfully imparts biodegradable cellulose paper as a

606 sustainable substitute for petroleum plastic films and exhibits great application
607 potential in active fresh fruit packaging.

608 **Acknowledgements**

609 This work was financially supported by the Natural Science Advance Research
610 Foundation of Shaanxi University of Science and Technology (2020XSGG-07), the
611 Key Research and Development Program of Shaanxi (Program No. 2022GY-278), the
612 Natural Science Basic Research Program of Shaanxi (Program No. 2023-JC-YB-104),
613 and the Foundation of Guangxi Key Laboratory of Clean Pulp & Papermaking and
614 Pollution Control (Program No. 2023GXZZKF36).

615 **Declarations of competing interest**

616 The authors declare no competing interests.

617 **Author contributions**

618 Fatima Ait Aissa: Conceptualization, Data curation, Formal analysis,
619 Methodology, Writing-original draft, Writing-review and editing; Xue Jiang:
620 Conceptualization, Funding acquisition, Project administration, Supervision,
621 Writing-review and editing; Xiuzhi Tian: Conceptualization, Funding acquisition,
622 Project administration, Supervision, Writing-review and editing.

623 **Data availability Statement**

624 The data supporting the results of this study are available from the corresponding
625 author upon reasonable request.

626 **References**

627 Alebachew, A. W., Abdalkarim, S. Y. H., Zhu, J., Wu, S., Zhang, Y., Yu, H.-Y., &

628 Yunusov, K. E. (2025). Two-directions mechanical strength and high-barrier
629 mechanisms of cellulose nanocrystal-based hybrids reinforced packaging with
630 nacre-mimetic structure. Carbohydrate Polymers, 348 (Part B), 122910.
631 https://doi.org/10.1016/j.carbpol.2024.122910.

632 Antlauf, M., Boulanger, N., Berglund, L., Oksman, K., & Andersson, O. (2021).
633 Thermal conductivity of cellulose fibers in different size scales and densities.
634 Biomacromolecules, 22(9), 3800–3809. https://doi.org/10.1021/acs.biomac.1c00643.

635 Apostolopoulou-Kalkavoura, V., Munier, P., & Bergström, L. (2020). Thermally
636 insulating nanocellulose-based materials. Advanced Materials, 33(28), 2001839.
637 https://doi.org/10.1002/adma.202001839.

638 Atykyan, N., Revin, V., & Shutova, V. (2020). Raman and FT-IR spectroscopy
639 investigation the cellulose structural differences from bacteria Gluconacetobacter
640 sucrofermentans during the different regimes of cultivation on a molasses media.
641 AMB Express, 10, 84. https://doi.org/10.1186/s13568-020-01020-8.

642 Ayub, A., Farrukh, S., Jan, R., Azeem, M., Salahuddin, Z., & Hussain, A. (2021). Gas
643 barrier properties evaluation for boron nitride nanosheets-polymer
644 (polyethylene-terephthalate) composites. Applied Nanoscience, 11(1), 91–99.
645 https://doi.org/10.1007/s13204-020-01563-z.

646 Biao, L., Tan, S., Meng, Q., Gao, J., Zhang, X., Liu, Z., & Fu, Y. (2018). Green
647 synthesis, characterization and application of proanthocyanidins-functionalized gold
648 nanoparticles. Nanomaterials, 8, 53. https://doi.org/10.3390/nano8010053.

649 Bunpheng, A., Saisopa, T., Iamprasertkun, P., Seubsai, A., Boonchun, A.,
650 Sirisaksoontorn, W., & Hirunpinyopas, W. (2025). Tuning physicochemical properties
651 of boron nitride-based membranes via scalable one-step exfoliation for ionic and
652 molecular nanofiltration. ACS Materials Au, 5(4), 687–697.
653 https://doi.org/10.1021/acsmaterialsau.5c00026.

654 Cao, J., Chen, L., Li, M., Cao, F., Zhao, L., & Su, E. (2018). Efficient extraction of
655 proanthocyanidin from Ginkgo biloba leaves employing rationally designed deep
656 eutectic solvent-water mixture and evaluation of the antioxidant activity. Journal of
657 Pharmaceutical and Biomedical Analysis, 158, 317–326.
658 https://doi.org/10.1016/j.jpba.2018.06.007.

659 Cazón, P., Morales-Sanchez, E., Velazquez, G., & Vázquez, M. Measurement of the
660 water vapor permeability of chitosan films: A laboratory experiment on food
661 packaging materials. Journal of Chemical Education, 99.
662 https://doi.org/10.1021/acs.jchemed.2c00449.

663 Chan, W. C., Kaseke, T., Chew, S. C., Neo, Y. P., & Nyam, K. L. (2025). Recent
664 advances in active, smart and edible packaging applications to enhance post-harvest
665 quality and shelf-life of fruits. Frontiers in Food Science and Technology, 5, 1723921.
666 https://doi.org/10.3389/frfst.2025.1723921.

667 Chandkiram Gautam, Selvam Chelliah. Methods of hexagonal boron nitride
668 exfoliation and its functionalization: covalent and non-covalent approaches. RSC Adv.
669 2021 Sep 23;11(50):31284–31327. https://doi.org/10.1039/d1ra05727h.

Chen, S., Xu, R., Liu, J., Zou, X., Qiu, L., Kang, F., Liu, B., & Cheng, H. M. (2019). Simultaneous production and functionalization of boron nitride nanosheets by sugar-assisted mechanochemical exfoliation. Advanced Materials, 31(10), e1804810. https://doi.org/10.1002/adma.201804810.

Dee, G., O'Donoghue, O., Rafferty, A., Gannon, L., McGuinness, C., & Gun'ko, Y. K. (2023). Boron nitride nanosheets functionalized with Fe3O4 and CoFe2O4 magnetic nanoparticles for nanofiltration applications. ACS Applied Nano Materials, 6, 5009–5018. https://doi.org/10.1021/acsanm.3c02375.

Dislaire, C., Grohens, Y., Seantier, B., & Muzy, M. (2021). The impact of molded pulp product process on the mechanical properties of molded bleached chemi-thermo-mechanical pulp. Functional Composite Materials, 2, 1–10. https://doi.org/10.1186/s42252-021-00020-2.

Gautam, C., & Chelliah, S. (2021). Methods of hexagonal boron nitride exfoliation and its functionalization: covalent and non-covalent approaches. RSC Advances, 11(50), 31284–31327. https://doi.org/10.1039/d1ra05727h.

Gerasimova, E., Gazizullina, E., Kolbaczkaya, S., & Ivanova, A. (2022). The novel potentiometric approach to antioxidant capacity assay based on the reaction with stable radical 2,2'-diphenyl-1-picrylhydrazyl. Antioxidants, 11(10), 1974. https://doi.org/10.3390/antiox11101974.

Gidado, M. J., Nagoor Gunny, A. A., Gopinath, S. C. B., Ali, A., Wongs-Aree, C., & Mohd Salleh, N. H. (2024). Challenges of postharvest water loss in fruits:

691 Mechanisms, influencing factors, and effective control strategies - A comprehensive
692 review. Journal of Agriculture and Food Research, 17, 101249.
693 https://doi.org/10.1016/j.jafr.2024.101249.

694 Grasel, F. dos S., Ferrão, M. F., & Wolf, C. R. (2016). Development of methodology
695 for identification the nature of the polyphenolic extracts by FTIR associated with
696 multivariate analysis. Spectrochimica Acta Part A: Molecular and Biomolecular
697 Spectroscopy, 153, 94–101. https://doi.org/10.1016/j.saa.2015.08.020.

698 Grzybek, P., Dudek, G., & van der Bruggen, B. (2024). Cellulose-based films and
699 membranes: A comprehensive review on preparation and applications. Chemical
700 Engineering Journal, 153500. https://doi.org/10.1016/j.cej.2024.153500.

701 Guerra, V., Wan, C., & McNally, T. (2019). Thermal conductivity of 2D
702 nano-structured boron nitride (BN) and its composites with polymers. Progress in
703 Materials Science, 100, 170–186. https://doi.org/10.1016/j.pmatsci.2018.10.002.

704 Hung, C., Hurst, J. B., Santiago, D., & Rogers, R. B. (2014). Exfoliation of hexagonal
705 boron nitride via ferric chloride intercalation. NASA Technical Reports Server.
706 https://ntrs.nasa.gov/api/citations/20140005373/downloads/20140005373.pdf.

707 Jha, S., Akula, B., Enyioma, H., Novak, M., Amin, V., & Liang, H. (2024).
708 Biodegradable biobased polymers: A review of the state of the art, challenges, and
709 future directions. Polymers, 16(16), 2262. https://doi.org/10.3390/polym16162262.

710 Jo, C., Rukmanikrishnan, B., Prabakaran, D. S., Ramalingam, S., & Lee, J. (2021).

711 Cellulose-pulp-based stretchable composite film with hydroxyethyl cellulose and
712 turmeric powder for packaging applications. ACS Sustainable Chemistry &
713 Engineering, 9(40), 13653–13662. https://doi.org/10.1021/acssuschemeng.1c05183.

714 Kathuria, A., & Zhang, S. (2022). Sustainable and repulpable barrier coatings for
715 fiber-based materials for food packaging: A review. Frontiers in Materials, 9.
716 https://doi.org/10.3389/fmats.2022.929501.

717 Kıvanç, M., Barutca, B., Koparal, A. T., Göncü, Y., Bostancı, S. H., & Ay, N. (2018).
718 Effects of hexagonal boron nitride nanoparticles on antimicrobial and antibiofilm
719 activities, cell viability. Materials Science and Engineering: C, 91, 115–124.
720 https://doi.org/10.1016/j.msec.2018.05.028.

721 Kolbl Repinc, S., Stres, B., Karlovits, M., Karlovits, I., Jerič, P., Panák, O., Verbič, A.,
722 Likozar, B., & Novak, U. (2024). Understanding bio-based polymers: A study of
723 origins, properties, biodegradation and their impact on health and the environment.
724 FEBS Open Bio. https://doi.org/10.1002/2211-5463.70183.

725 Kostoglou, N., Polychronopoulou, K., & Rebholz, C. (2014). Thermal and chemical
726 stability of hexagonal boron nitride (h-BN) nanoplatelets. Vacuum, 112, 42–45.
727 https://doi.org/10.1016/j.vacuum.2014.11.009.

728 LakshmiBalasubramaniam, S., Patel, A. S., Nayak, B., Howell, C., & Skonberg, D.
729 (2021). Antioxidant and antimicrobial modified cellulose nanofibers for food
730 applications. Food Bioscience, 44(Part A), 101421.
731 https://doi.org/10.1016/j.fbio.2021.101421.

Li, J., Zhang, X., Zhou, W., Tu, Z., Yang, X., Hao, J., Liang, F., Chen, Z., & Du, Y. (2023). Impacts of proanthocyanidin binding on conformational and functional properties of decolorized Highland barley protein. Foods, 12(3), 481. https://doi.org/10.3390/foods12030481.

Li, J., Lin, J., Xu, X., Zhang, X., Xue, Y., Mi, J., Mo, Z., Fan, Y., Hu, L., Yang, X., Zhang, J., Meng, F., Yuan, S., & Tang, C. (2013). Porous boron nitride with a high surface area: Hydrogen storage and water treatment. Nanotechnology, 24(15), 155603. https://doi.org/10.1088/0957-4484/24/15/155603.

Li, S., Lu, X., Lou, Y., Liu, K., & Zou, B. (2021). The synthesis and characterization of h-BN nanosheets with high yield and crystallinity. ACS Omega, 6(42), 27814–27822. https://doi.org/10.1021/acsomega.1c03406.

Li, W., Wang, S., Wang, W., et al. (2019). Facile preparation of reactive hydrophobic cellulose nanofibril film for reducing water vapor permeability (WVP) in packaging applications. Cellulose, 26, 3271–3284. https://doi.org/10.1007/s10570-019-02270-x.

Liu, M., & Wang, Y. (2026). Hexagonal boron nitride nanosheets: Properties, preparation and applications in thermal management. Nanomaterials, 16(2), 101. https://doi.org/10.3390/nano16020101.

Liu, W., Ullah, B., Kuo, C., & Cai, X. (2019). Two-dimensional nanomaterials-based polymer composites: Fabrication and energy storage applications. Advances in Polymer Technology, 2019, 1–15. https://doi.org/10.1155/2019/4294306.

752 Liu, Y., Zhang, Y., Liao, T., Gao, L., Wang, M., Xu, X., Yang, X., & Liu, H. (2020).
753 Boron nitride-nanosheet enhanced cellulose nanofiber aerogel with excellent thermal
754 management properties. Carbohydrate Polymers, 241, 116425.
755 https://doi.org/10.1016/j.carbpol.2020.116425.

756 Lufu, R., Ambaw, A., & Opara, U. L. (2020). Water loss of fresh fruit: Influencing
757 pre-harvest, harvest and postharvest factors. Scientia Horticulturae, 272, 109519.
758 https://doi.org/10.1016/j.scienta.2020.109519.

759 Mahajan, B. V. C., Dhillon, W. S., Kumar, M., & Singh, B. (2014). Effect of different
760 packaging films on shelf life and quality of peach under super and ordinary market
761 conditions. Journal of Food Science and Technology, 52(6), 3756–3762.
762 https://doi.org/10.1007/s13197-014-1382-y.

763 Mannan, M. A., Nagano, M., Shigezumi, K., Kida, T., Hirao, N., & Baba, Y. (2008).
764 Characterization of boron carbonitride (BCN) thin films deposited by radiofrequency
765 and microwave plasma enhanced chemical vapor deposition. American Journal of
766 Applied Sciences, 5(6), 736–741. https://doi.org/10.3844/ajassp.2008.736.741.

767 Mohamed, S. A. A., El-Sakhawy, M., & Diab, M. A. (2025). Enhancement of bagasse
768 paper properties for sustainable packaging via bentonite and alginate loading in
769 shellac coatings. Scientific Reports, 15(1), 39412.
770 https://doi.org/10.1038/s41598-025-22179-9.

771 Mujtaba, M., Lipponen, J., Ojanen, M., Puttonen, S., & Vaittinen, H. (2022). Trends
772 and challenges in the development of bio-based barrier coating materials for

773 paper/cardboard food packaging; a review. Science of The Total Environment, 851,
774 158328. https://doi.org/10.1016/j.scitotenv.2022.158328.

775 Ncube, L. K., Ude, A. U., Ogunmuyiwa, E. N., Zulkifli, R., & Beas, I. N. (2020).
776 Environmental impact of food packaging materials: A review of contemporary
777 development from conventional plastics to polylactic acid based materials. Materials,
778 13(21), 4994. https://doi.org/10.3390/ma13214994.

779 Nian, L., Wang, M., Sun, X., Zeng, Y., Xie, Y., Cheng, S., & Cao, C. (2024).
780 Biodegradable active packaging: Components, preparation, and applications in the
781 preservation of postharvest perishable fruits and vegetables. Critical Reviews in Food
782 Science and Nutrition, 64(8), 2304–2339.
783 https://doi.org/10.1080/10408398.2022.2122924.

784 Nie, F., Liu, L., Cui, J., Zhao, Y., Zhang, D., Zhou, D., Wu, J., Li, B., Wang, T., Li, M.,
785 & Yan, M. (2023). Oligomeric proanthocyanidins: An updated review of their natural
786 sources, synthesis, and potentials. Antioxidants, 12(5), 1004.
787 https://doi.org/10.3390/antiox12051004.

788 Oh, S. Y., Yoo, D. I., Shin, Y., & Seo, G. (2005). FTIR analysis of cellulose treated
789 with sodium hydroxide and carbon dioxide. Carbohydrate Research.
790 https://doi.org/10..1016/j.carres.2004.11.027.

791 Park, S., Baker, J. O., Himmel, M. E., Parilla, P. A., & Johnson, D. K. (2010).
792 Cellulose crystallinity index: Measurement techniques and their impact on
793 interpreting cellulase performance. Biotechnology for Biofuels, 3, 10.

https://doi.org/10.1186/1754-6834-3-10.

Peng, Y., Yang, Y., Xiao, K., Yang, Y., Ding, H., Deng, J., & Sun, W. (2023). Direct synthesis of vertical self-assembly oriented hexagonal boron nitride on gallium nitride and ultrahigh photoresponse ultraviolet photodetectors. Nanomaterials, 13(9), 1546. https://doi.org/10.3390/nano13091546.

Qadir, A., Le, T. K., Malik, M., Amedome Min-Dianeye, K. A., Saeed, I., Yiting, & Choi, J. R. (2021). Representative 2D-material-based nanocomposites and their emerging applications: A review. RSC Advances, 11, 23860–23880. https://doi.org/10.1039/D1RA03425A.

Rajwar, A., Srivastava, P., & Sahgal, M. (2016). Microbiology of fresh produce: Route of contamination, detection methods, and remedy. Critical Reviews in Food Science and Nutrition, 56(14), 2383–2390. https://doi.org/10.1080/10408398.2013.841119.

Rasul, M. G., Kiziltas, A., Arfaei, B., & Shahbazian-Yassar, R. (2021). 2D boron nitride nanosheets for polymer composite materials. npj 2D Materials and Applications, 5(1). https://doi.org/10.1038/s41699-021-00231-2.

Rauf, A., Imran, M., Abu-Izneid, T., Iahtisham-Ul-Haq, Patel, S., Pan, X., Naz, S., Sanches Silva, A., Saeed, F., & Suleria, H. A. R. (2019). Proanthocyanidins: A comprehensive review. Biomedicine & Pharmacotherapy, 116, 108999. https://doi.org/10.1016/j.biopha.2019.108999.

814 Rbihi, S., Laallam, L., Sajieddine, M., & Jouaiti, A. (2019). Characterization and
815 thermal conductivity of cellulose based composite xerogels. Heliyon, 5(5), e01704.
816 https://doi.org/10.1016/j.heliyon.2019.e01704.

817 Roudi, M. R. R., Hosseini, A., Ranjkesh, M., Pan, Z., & Korayem, A. H. (2024).
818 Dispersion stability and the reaction mechanism of boron nitride nanosheets in a
819 cementitious alkaline environment. ACS Applied Nano Materials, 7(11), 12592–
820 12604. https://doi.org/10.1021/acsanm.4c01082.

821 Rue, E. A., Rush, M. D., & van Breemen, R. (2017). Procyanidins: A comprehensive
822 review encompassing structure elucidation via mass spectrometry. Phytochemistry
823 Reviews, 17(1), 1–16. https://doi.org/10.1007/s11101-017-9507-3.

824 Itskou, J., L'Hermitte, A., Marchesini, S., Tian, T., & Petit, C. (2023). How to tailor
825 porous boron nitride properties for applications in interfacial processes. Accounts of
826 Materials Research, 4, 143–155. https://doi.org/10.1021/acs.accounts.3c00308.

827 Sangroniz, A., Zhu, J., Tang, X., Etxeberria, A., Chen, E. Y., & Sardon, H. (2019).
828 Packaging materials with desired mechanical and barrier properties and full chemical
829 recyclability. Nature Communications, 10(1), 3559.
830 https://doi.org/10.1038/s41467-019-11525-x.

831 Santmarti, A., Liu, H. W., Herrera, N., & Lee, K. Y. (2020). Anomalous tensile
832 response of bacterial cellulose nanopaper at intermediate strain rates. Scientific
833 Reports, 10(1), 15260. https://doi.org/10.1038/s41598-020-72153-w.

834 Santos, J., Moschetta, M., Rodrigues, J., Alpuim, P., & Capasso, A. (2021).
835 Interactions between 2D materials and living matter: A review on graphene and
836 hexagonal boron nitride coatings. Frontiers in Bioengineering and Biotechnology, 9,
837 612669. https://doi.org/10.3389/fbioe.2021.612669.

838 Santos-Buelga, C., & Scalbert, A. (2000). Proanthocyanidins and tannin-like
839 compounds - nature, occurrence, dietary intake and effects on nutrition and health.
840 Journal of the Science of Food and Agriculture, 80(7), 1094–1117.
841 https://doi.org/10.1002/(sici)1097-0010(20000515)80:7.

842 Shams, M., Mansukhani, N., Hersam, M. C., Bouchard, D., & Chowdhury, I. (2023).
843 Environmentally sustainable implementations of two-dimensional nanomaterials.
844 Frontiers in Chemistry, 11. https://doi.org/10.3389/fchem.2023.1132233.

845 Siddiqui, S. A., Yang, X., Deshmukh, R. K., Gaikwad, K. K., Bahmid, N. A., &
846 Castro-Muñoz, R. (2024). Recent advances in reinforced bioplastics for food
847 packaging - A critical review. International Journal of Biological Macromolecules,
848 263, 130399. https://doi.org/10.1016/j.ijbiomac.2024.130399.

849 Stepina, I., Zhukov, A., & Bazhenova, S. (2023). Modification of cellulosic materials
850 with boron-nitrogen compounds. *Polymers*, 15(13), 2788.
851 https://doi.org/10.3390/polym15132788.

852 Stoica, M., Bichescu, C. I., Crețu, C. M., Dragomir, M., Ivan, A. S., Podaru, G. M.,
853 Stoica, D., & Stuparu-Crețu, M. (2024). Review of bio-based biodegradable polymers:
854 Smart solutions for sustainable food packaging. Foods, 13(19), 3027.

855 https://doi.org/10.3390/foods13193027.

856 Tang, J., Chen, L., Yan, D., Shen, Z., Wang, B., Weng, S., Wu, Z., Xie, Z., Shao, J.,
857 Yang, L., & Shen, L. (2020). Surface functionalization with proanthocyanidins
858 provides an anti-oxidant defense mechanism that improves the long-term stability and
859 osteogenesis of titanium implants. SHILAP Revista de Lepidopterología.
860 https://doaj.org/article/d324c5aa7a76452083b2ab6cc1d89392.

861 Tian, X., Li, Y., Chen, Z., Li, Q., Hou, L., Wu, J., Tang, Y., & Li, Y. (2017).
862 Shear-assisted production of few-layer boron nitride nanosheets by supercritical CO2
863 exfoliation and its use for thermally conductive epoxy composites. Scientific Reports,
864 7(1), 17794. https://doi.org/10.1038/s41598-017-18149-5.

865 Tian, X., Xiao, J., Bai, H., Ait Aissa, F., Li, W., Zhao, D., & Jiang, X. (2025).
866 Nanocomposites of chito-oligosaccharide grafted boron nitride
867 nanosheets/carboxymethyl cellulose for thermal management of flexible electronic
868 devices. Cellulose. https://doi.org/10.1007/s10570-025-06790-7.

869 Wang, M., Chen, J., Chen, S., Ye, X., & Liu, D. (2021). Inhibition effect of three
870 common proanthocyanidins from grape seeds, peanut skins and pine barks on maize
871 starch retrogradation. Carbohydrate Polymers, 252, 117172.
872 https://doi.org/10.1016/j.carbpol.2020.117172.

873 Wang, R., Zhang, F., Yang, K., Xiong, Y., Tang, J., Chen, H., Duan, M., Li, Z., Zhang,
874 H., & Xiong, B. (2023). Review of two-dimensional nanomaterials in tribology:
875 Recent developments, challenges and prospects. Advances in Colloid and Interface

876 Science, 321, 103004. https://doi.org/10.1016/j.cis.2023.103004.

877 Wu, N., Yang, W., Che, S., Sun, L., Li, H., Ma, G., Sun, Y., Liu, H., Wang, X., & Li, Y.
878 (2022). Green preparation of high-yield and large-size hydrophilic boron nitride
879 nanosheets by tannic acid-assisted aqueous ball milling for thermal management.
880 Composites Part A: Applied Science and Manufacturing, 164, 107266.
881 https://doi.org/10.1016/j.compositesa.2022.107266.

882 Xu, X., Su, Y., Zhang, Y., Wu, S., Wu, K., & Fu, Q. (2020). A dual-crosslinked and
883 anisotropic regenerated cellulose/boron nitride nanosheets film with high thermal
884 conductivity, mechanical strength, and toughness. Frontiers in Bioengineering and
885 Biotechnology, 8, 602318. https://doi.org/10.3389/fbioe.2020.602318.

886 Xu, Z., Du, P., Meiser, P., & Jacob, C. (2012). Proanthocyanidins: Oligomeric
887 structures with unique biochemical properties and great therapeutic promise. Natural
888 Product Communications, 7(3), 381–388.
889 https://doi.org/10.1177/1934578x1200700321.

890 Yang, X., Zhao, B., Ji, L., Hu, P., Zhu, X., & Li, Z. (2023). Novel functionalized
891 boron nitride nanosheets achieved by radiation-induced oxygen radicals and their
892 enhancement for polymer nanocomposites. Molecules, 28(8), 3444.
893 https://doi.org/10.3390/molecules28083444.

894 Ye, C., Li, X., & Chen, J. (2026). High-temperature sintering behavior and
895 microstructural evolution of boron nitride nanosheet composite Si–Al–C–O fibers.
896 International Journal of Applied Ceramic Technology.

https://doi.org/10.1111/ijac.70175.

Yin, Y., & Woo, M. W. (2024). Transitioning of petroleum-based plastic food packaging to sustainable bio-based alternatives. Sustainable Food Technology, 2(3), 548–566. https://doi.org/10.1039/d4fb00028e.

Yu, A., Sun, L., Chen, L., Wang, D., Li, Z., Wang, Y., Wang, Z., & Lin, S. (2025). The biological functions of proanthocyanidin and its application in pig production. Frontiers in Veterinary Science, 12, 1565501. https://doi.org/10.3389/fvets.2025.1565501.

Yu, Y., Cui, M., Zheng, W., & Zhao, H. (2022). Eco-friendly functionalization of hexagonal boron nitride nanosheets with carbon dots towards reinforcement of the protective performance of water-borne epoxy coatings. New Journal of Chemistry, 46(13), 6330–6342. https://doi.org/10.1039/d2nj00310d.

Yu, Y., Sun, M., Han, P., Shang, H., Zhang, S., & Sun, B. (2026). Large-scale semisynthesis of bioactive procyanidin B2 3,3′-di-O-gallate: Structural characterization, simulated in vitro digestion, and protective effects against colitis. Journal of Agricultural and Food Chemistry. https://doi.org/10.1021/acs.jafc.5c14079.

Zang, J., Lv, Z., Yang, C., Zhang, T., Wang, Y., Wang, D., & Liu, H. (2026). Functionalized boron nitride nanomaterials: Exploring antioxidant and antitumor activities for advanced therapeutic applications. iScience, 29(5), 115546. https://doi.org/10.1016/j.isci.2026.115546.

Zhang, Z., Du, J., Li, J., Huang, X., Kang, T., Zhang, C., Wang, S., Ajao, O. O., Wang, W., & Liu, P. (2021). Polymer nanocomposites with aligned two-dimensional materials. Progress in Polymer Science, 114, 101360. https://doi.org/10.1016/j.progpolymsci.2021.101360.

Zheng, C., Lyu, G., Janaswamy, S., Yang, G., Guo, Z., & Ji, X. (2026). High-strength, high-barrier active packaging films from lignin-compatibilized cellulose and beeswax. Food Packaging and Shelf Life, 55, 101739. https://doi.org/10.1016/j.fpsl.2026.101739.

Zhou, L., Zhang, B., Li, F., Yan, Y., Wang, Y., & Li, R. (2023). Preparation of boron nitride nanosheets by glucose-assisted ultrasonic cavitation exfoliation. Nanoscale Advances, 5(23), 6582–6593. https://doi.org/10.1039/d3na00737e.

Supplementary Files

This is a list of supplementary files associated with this preprint. Click to download.

- SupportingInformationfinalversion.docx